CIGRE 2025 International Symposium
Palais des Congrès de Montréal, Québec, Canada
September 29 to October 3, 2025

10520
EHV&UHV AC and DC
PS3: Climate Change and Extreme Weather Events

Identification of At-Risk Substations in the German Transmission Grid from Space Weather

Aline GUIMARÃES CARVALHO	Leonie PICK	Alexander GRAYVER	Stefan TENBOHLEN
German Aerospace Center Germany	German Aerospace Center Germany	University of Cologne Germany	University of Stuttgart Germany
aline.guimaraescarvalho@dlr.de	leonie.pick@dlr.de	agrayver@uni-koeln.de	stefan.tenbohlen@ieh.uni-stuttgart.de

SUMMARY

Geomagnetically induced currents (GICs) are a space weather phenomenon resulting from natural geomagnetic disturbances and have the potential to cause the malfunction of grounded power systems. GICs are considered quasi-direct currents (DC) and can lead to half-cycle saturation in transformers. The impacts of these currents on the German power grid remain uncertain due to the lack of Germany-wide estimates or measurements. To address this gap, GICs were modelled in the German transmission grid for two geomagnetic storms: one in April 2023 and another in May 2024. These storms provide valuable cases for analysing GIC behaviour under different space weather conditions. This study highlights that the spatial distribution of high GICs does not only depend on the geomagnetic fields but is also heavily influenced by the overall configuration and orientation of connected lines. Substations that exhibit maximum GIC amplitudes in the top 5% during both events were identified as high-risk stations.

KEYWORDS

Geomagnetically Induced Currents, High Voltage, Power Grids, Space Weather

1 Introduction

Geomagnetically Induced Currents (GICs) are parasitic currents that arise in ground-based conductors as a result of rapid external geomagnetic field variations during geomagnetic storms [1]. These currents can flow through critical infrastructure, such as high-voltage (HV) power transmission networks, pipelines, and railways, potentially causing disruptions and damage with significant economic losses [2].

The temporal variation of the magnetic field associated with geomagnetic storms induces an electric field in the electrically conductive subsurface (Faraday's Law of induction). When the electric field interacts with grounded power systems, an electromotive force is generated in the power lines and acts as an additional voltage source, initiating the flow of GICs [3].

GICs behave as quasi-direct currents (DC) relative to the power grid frequency (50 Hz in Germany), due to their low frequencies ($\leq$ 1 Hz). When flowing through transformers, they may shift their operating point from the linear region of the magnetization curve to the saturation region, a process known as half-cycle saturation [4]. This shift leads to a sharp increase in the excitation currents and causes non-linear behaviour, resulting in a higher reactive power demand and generation of both even and odd harmonics. These effects can lead to transformer overheating, false operation of protective relays, and voltage instability [4].

Several incidents have shown the vulnerability of power systems to strong geomagnetic storms. During the Halloween Storm in 2003, for instance, GIC-related impacts were observed at mid and even at low geomagnetic latitudes, including in South Africa [5].

In Germany, the presence of GICs has been confirmed through direct current (DC) measurements at transformer neutral points [6]. However, the behaviour of GICs across the German power grid remains poorly understood. To address this gap, we modelled GICs in the German power grid for two geomagnetic storms: one in April 2023 and another in May 2024 with the aim to identify substations that are exposed to increased risk.

2 GIC modelling

The modelling of GICs can be divided into two main sections: the geophysical part and the power engineering part. In the former, the geoelectric field at the Earth's surface is estimated based on INTERMAGNET measurements of the magnetic field during the selected geomagnetic storms and a conductivity model of the Earth’s subsurface. The focus of this study is the engineering part, in which the geoelectric field is used to evaluate GICs at specific locations and components within the power grid.

2.1 Geomagnetic storm events and induced electric field

One-minute resolved measurements of the horizontal magnetic field, denoted $\vec{B}(\mathrm{t})$, whose components relate to the geodetic North (B_x) and the geodetic East (B_y), were obtained from up to 10 observatories located in and around Germany. The induced electric field is then computed by following the methodology outlined in [6]. Instead of the 1-D surface plane-wave scalar impedance, we now employ a full plane-wave impedance tensor computed for a dedicated 3-D conductivity model. The model consists of a 3-D top layer (15 km thick) over a homogeneous crust of 100 Ωm and a 1-D conductivity mantle profile underneath [7]. The top

layer combines ocean/sea water and marine sediments [8] with land sediments [9] and enables the calculation of a realistic impedance tensor near the coast. The plane-wave impedance tensor response of this model is then computed on a log-spaced set of frequencies over a dense surface grid (~0.025° spacing) by using the electromagnetic 3-D solver GoFEM [10].

The first geomagnetic storm to be analysed occurred in April 2023 (Event 1; analysis period: 00:00 on 23 April to 00:00 on 26 April). The calculated GIC could be validated at a substation in northwest Germany, where DC measurements at the transformer neutral point were available for comparison [6]. The second event, also named the "Mother's Day Storm", happened in May 2024 (Event 2; analysis period: 00:00 on 10 May to 00:00 on 13 May 2024) and is classified as an extreme geomagnetic storm, being reported as the most intense since the Halloween Storm of 2003 [11].

Figure 1 depicts 24-hour periods of the Hp30 index, which describes the intensity of the global geomagnetic activity [12]. Also shown is the derivative of the horizontal magnetic field $d\vec{B}/dt$, given its close relation to GICs [13], and the induced electric field $\vec{E}$, evaluated at the substations where the maximum $\vec{E}$ components are estimated: *Streumen* for Event 1 ($E_x = 0.12\,V/km$) and *Eula* for Event 2 ($E_y = 0.32\,V/km$), labelled J and K in Figure 4, respectively.

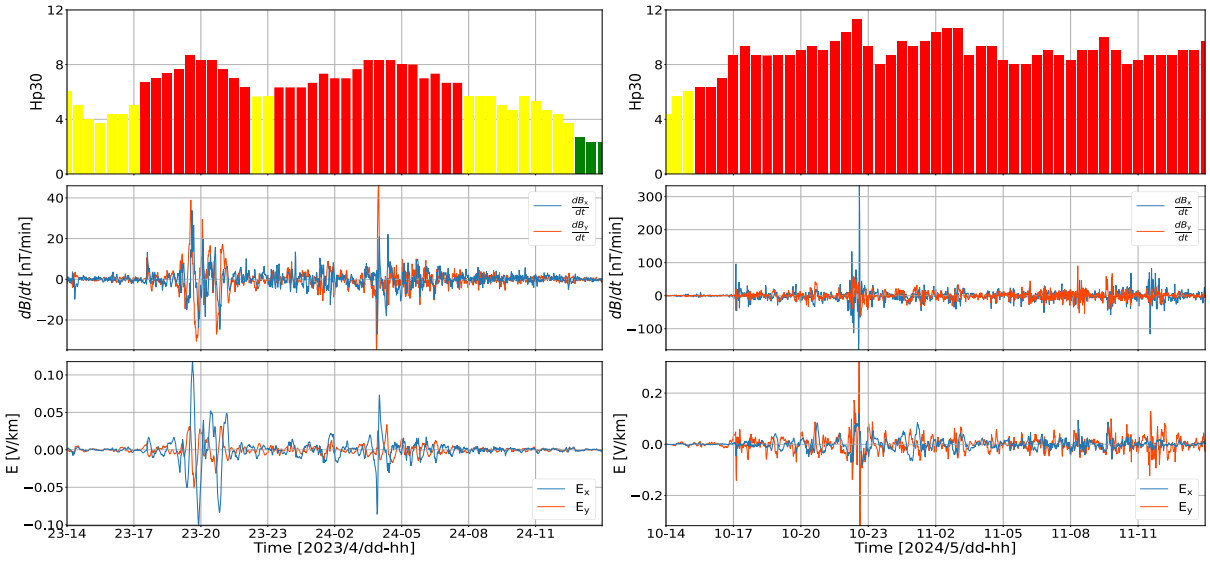

***Figure 1** – From top to bottom: Hp30 index, magnetic field derivative and electric field at substations where $\vec{E}$ peaks for (a) Event 1 in April 2023 and (b) Event 2 in May 2024.*

2.2 German transmission network

In order to calculate GICs in power grids, it is essential to have data on transmission lines, substations, transformers and the network topology. The geographic location of substations and line routes, along with the grounding points of the grid, must be known. As GICs are considered to behave as quasi-DC, only resistance values are needed for the calculations.

In the present study, the extra-high voltage levels of 220 kV and 380 kV within the German transmission grid are considered. Data on line resistances, their connections, and on some of the substations are provided in the Static Grid Model (SGM) of the Joint Allocation Office [14], which is updated biannually.

The SGM does not provide all the necessary information. When data are lacking, the grounding resistance of the substation is assumed as 0.1 Ω, and the transformer winding resistances are derived from the values specified in [15]. Geographic coordinates of the substations are retrieved from the OpenStreetMap database and the routes of the transmission lines are simplified as straight lines. Transformers are assumed to be Y–Y connected if the substation has lines of both voltage levels connected to it. Additionally, one earthed transformer per substation is considered.
The model includes a total of 771 lines for SGM 2023 and 779 lines for SGM 2024, as well as 375 transformers in both versions. The reported number of lines accounts for all identified connections, including cases where multiple lines link the same substations. Including the connections with neighbouring countries in the network would require extending the current $\vec{E}$ modelling scheme beyond Germany, which is planned for future work.

2.3 GIC calculation

The electromotive force (EMF) generated by the geoelectric field can be modelled as a DC voltage source in series with the transmission line,

$$V(\mathrm{t}) = \int_R \vec{E}_l(t) \cdot \overrightarrow{dl} \cong E_x(t)L_x + E_y(t)L_y \,, \tag{1}$$

where $\vec{E}_l$ refers to the electric field along the line, $\overrightarrow{dl}$ the incremental line segment and R the geographical route of the line. While $\vec{E}_l$ is typically spatially non-uniform, calculations can be simplified assuming a uniform electric field within small segments (right-hand side), where E_x (E_y) and L_x (L_y) correspond to the electric field component and distance between substations in the northward (eastward) direction. Once the induced voltages for all lines in the grid are determined and the nodal admittance matrix is built using the resistance values representing the grid, the GIC at each node can be calculated by applying Kirchhoff's current law (details in [3]).

3 GIC modelling results

GICs were modelled for both storms as described in Section 2. Initially, SGM 2023 was employed for Event 1, as it corresponds to the version closest in date to the event. However, it was observed that differences between SGM versions could influence the GIC results. Subsequently, SGM 2024 was also tested for comparison.
Figure 2 shows snapshots of GICs calculated at the transformer neutral points for all substations at the time of maximum observed GIC amplitude. The $\vec{E}$ (red) and $\vec{B}$ (blue) vectors at the substations with the top 10% electric field amplitudes are also illustrated. The substations with the top 5% of GIC amplitudes are shown in salmon, while the substation with the maximum amplitude is highlighted in orange. The location and timing of the maximum GIC depend on the SGM version: for SGM 2023, the highest GIC amplitude is observed at substation *Stendal/West*, whereas SGM 2024 yields a maximum at substation *Klixbüll/Süd*.
The percentage change in the maximum GIC amplitude is calculated for all substations within the storm time window. Only some substations show substantial deviations. One example is *Hardegsen* (substation *F* in Figure 4), which experiences a 230% increase in its maximum GIC amplitude. Such large changes are attributed to differences in network connectivity, e.g., in the

case of *Hardegsen*, we found that a connected line in SGM 2023 is absent in SGM 2024.

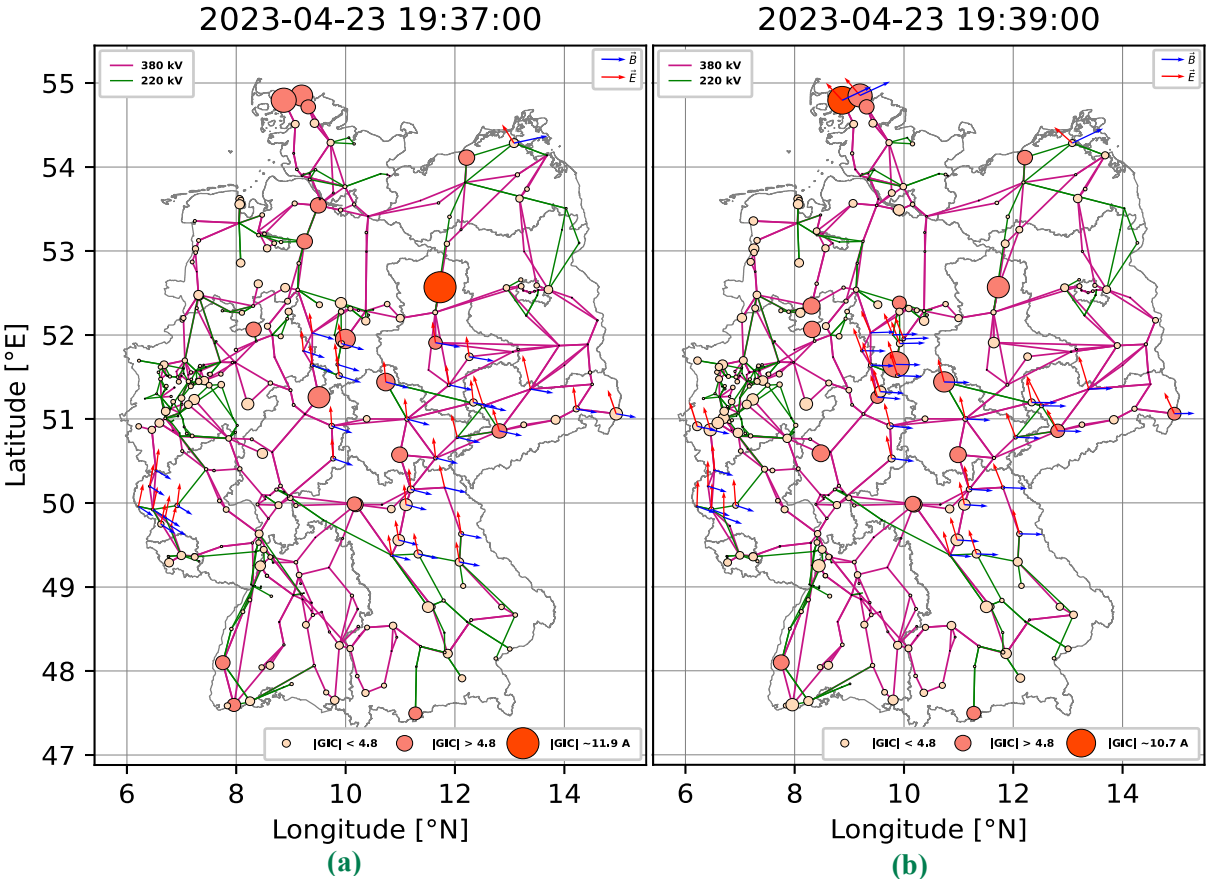

***Figure 2** – GIC distribution at the time of maximum amplitude for Event 1. (a) SGM 2023 (b) SGM 2024. Circle diameters are proportional to |GIC|, while arrow lengths represent the magnitudes of $\vec{B}$ (blue) and $\vec{E}$ (red). The displayed GICs correspond to three-phase currents*

Despite these differences, the overall mean, median, and standard deviation of the maximum GIC across all substations remain relatively stable with changes of 1.33%, 0.86% and 2.19%, respectively. This suggests that the primary effect of the changing grid configuration is on the spatial distribution of GIC amplitudes rather than the total current in the system. In other words, although the GIC amplitude at individual substations may increase or decrease, the overall energy input from the geomagnetic storm remains nearly constant.

Following the same approach, GICs were modelled for Event 2 with SGM 2024, producing time series for all substations in the grid over the studied period. Figure 3 presents a snapshot of GIC amplitudes for Event 2, in the same format as in Figure 2. Here, the largest GIC amplitude was observed at the substation *Ragow*.

Table 1 presents the maximum values of GIC, $d\vec{B}/dt$ and $\vec{E}$ at the time of maximum GIC for both events. The two storms are compared based on GICs calculated using the SGM 2024. Since the maximum GIC amplitude observed at different points in the grid does not occur simultaneously for each event, the highest GIC value observed at each substation over the entire time series is considered, rather than a single snapshot. Figure 4 presents maps showing the maximum GIC amplitudes at all substations during the respective storm periods. Additionally, the top 10% of the $d\vec{B}/dt$ and $\vec{E}$ are illustrated, corresponding to the times when the GIC maxima occur at each substation.

Table 1 – Maximum GIC, B and E values and occurrence time for Event 1 and 2

SGM	Max |GIC|	time	Substation	dB/dt $[nT/min]$		E $[V/km]$	
				X	Y	X	Y
2023	11.90	23.04.2023 19:37	Stendal/West	47.66	35.30	0.05	-0.01
2024	10.69	23.04.2023 19:39	Klixbüll/Süd	37.39	19.34	0.06	-0.05
2024	24.83	10.05.2024 22:36	Ragow	-151.39	-3.77	0.04	0.14

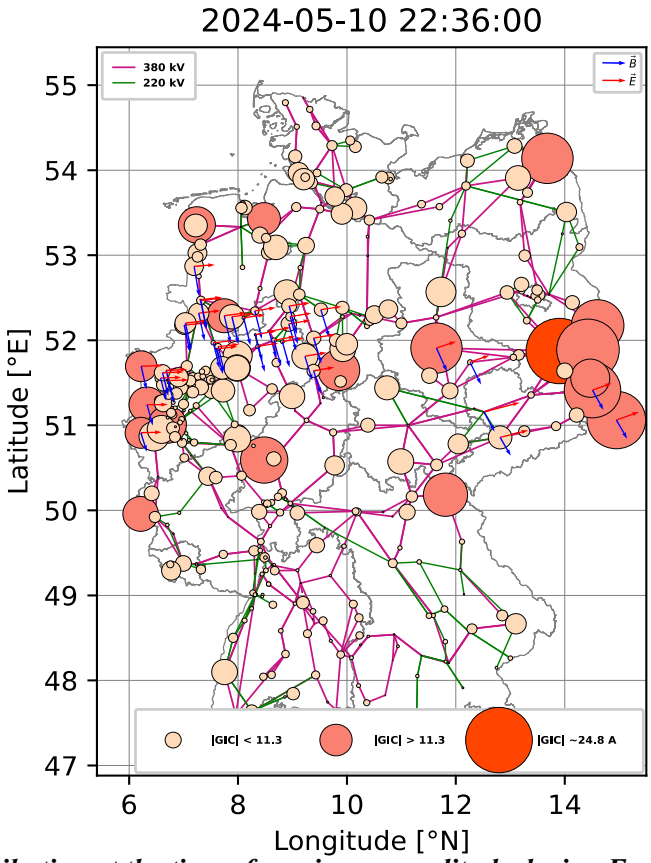

Figure 3 – GIC distribution at the time of maximum amplitude during Event 2. Circle diameters are proportional to |GIC|, while arrow lengths represent the magnitudes of $\vec{B}$ (blue) and $\vec{E}$ (red). The displayed GICs correspond to three-phase currents

Table 2 summarises statistical parameters for all substations shown on the map, including maximum, median and 95th percentile GICs, along with magnitudes of $d\vec{B}/dt$ and $\vec{E}$. Comparing Event 1 to Event 2, both the maximum and median values of $d\vec{B}/dt$ increase more than 300%, while $\vec{E}$ rises by about 120%. The maximum GIC increases by 132%, and the median by approximately 70%. As expected, $\vec{E}$ does not increase linearly with $d\vec{B}/dt$ due to the complex conductivity structure of the Earth's subsurface. Similarly, GIC amplitudes do not scale proportionally, as they are influenced by the topology of the power grid.

Table 2 – Comparison of |GIC|, $|d\vec{B}/dt|$ and $|\vec{E}|$ between Events 1 and 2

Event	|GIC|			$\|d\vec{B}/dt\|$ $[nT/min]$		$\|\vec{E}\|$ $[V/km]$	
	Max	Median	95th perc.	Max	Median	Max	Median
1: April 2023	10.69	1.95	5.60	71.23	36.73	0.11	0.06
2: Mai 2024	24.83	3.36	12.51	392.49	147.24	0.25	0.12
Increase (%)	132.27	71.77	123.43	451.00	300.89	120.68	121.42

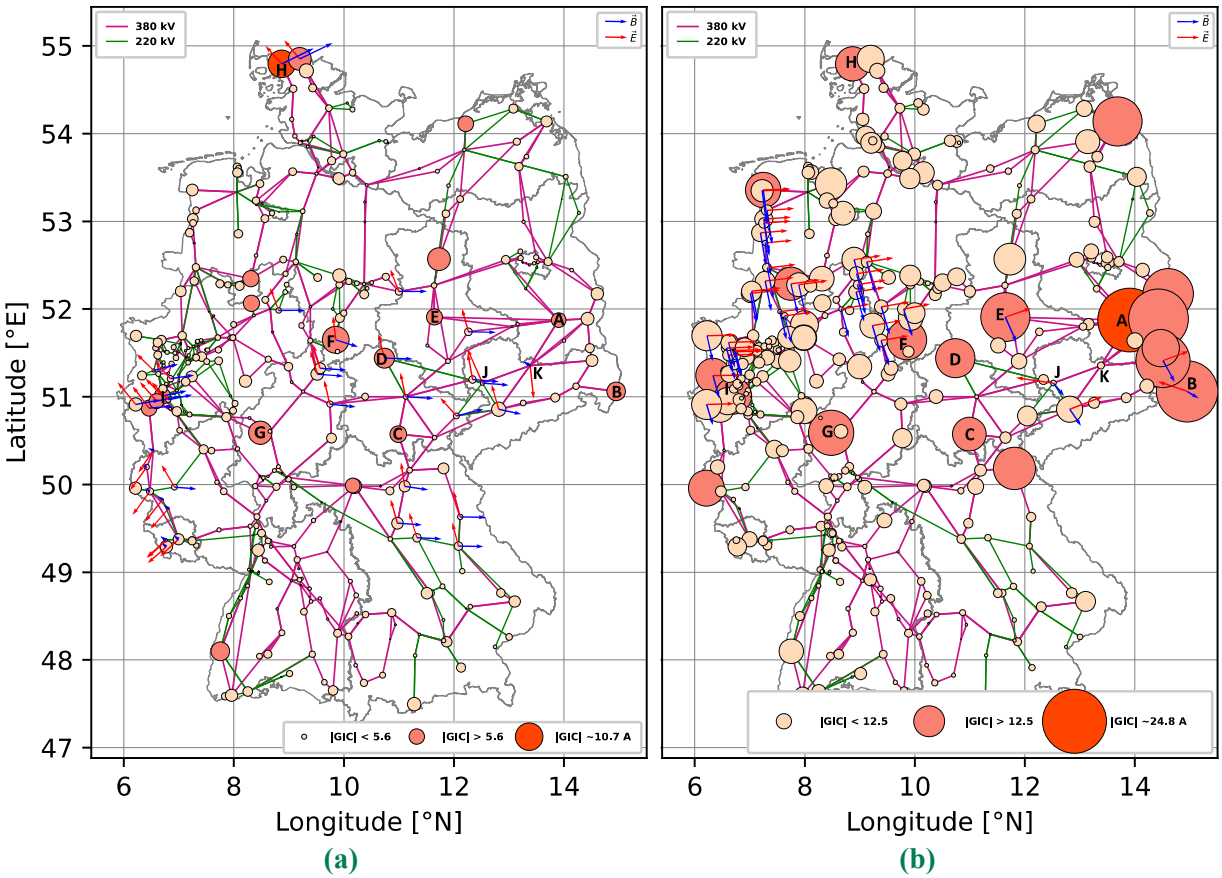

***Figure 4** – Maximum |GIC| observed for (a) Event 1 and (b) Event 2. Circle diameters are proportional to |GIC|, while arrow lengths represent to the magnitudes of $\vec{B}$ (blue) and $\vec{E}$ (red). The displayed GICs correspond to three-phase currents.*

4 Discussion and Conclusions

This study presents the first GIC results for Germany as a whole, based on two geomagnetic storms. Event 2 (May 2024) exhibits a stronger intensity than Event 1 (April 2023), as summarized in Table 2. The $\vec{B}$ and $\vec{E}$ vectors presented in Figures 2-4 illustrate how the electromagnetic field varies in magnitude and direction not only throughout a single storm (Figures 2a, 2b) but also between the two events. For Event 1, the maximum |GIC| at each substation (see Figure 4) is correlated better with the northward component of $\vec{E}$ at the corresponding time and location than with the eastward component (Pearson correlation coefficient of 0.28 for E_x vs. 0.03 for E_y). For Event 2, it is the other way around (0.09 for E_x vs. 0.38 for E_y). This is consistent with the different predominant orientations of $\vec{E}$ for the two selected events and confirms that vastly different alignment scenarios between the induced electric field and the power lines must be considered.

Among the 19 top 5% substations with the largest maximum GIC, 9 are common to both events (indexed in Figure 4). Of these, 4 substations (for Event 1) and 2 stations (for Event 2) also experience $\vec{E}$ magnitudes within the top 10%. Table 3 presents a zoomed-in map view of the 9 substations, additionally including substation *J*, showing the orientation of the connected lines, along with $\vec{E}$ vectors (purple for Event 1, red for Event 2).

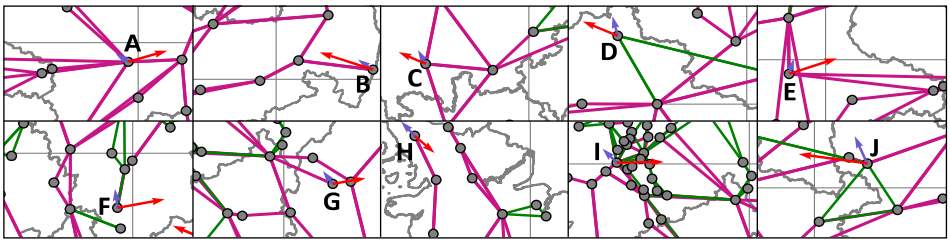

Figure 5 – Substations where max. |GIC| > 95th percentile for both events. $\vec{E}$ is illustrated for Event 1 (purple) and for Event 2 (red)

Table 3 presents the maximum GIC and $\vec{E}$ magnitudes at those substations, along with substation parameters and maximum GICs evaluated in the lines connected to these substations at the time of the GIC peak. With exception of *D*, all of these substations are connected to 380 kV lines, which likely contributes to the higher GICs there [16]. In most cases, at least one of the connected lines is oriented such that its angle with $\vec{E}$ is small (< 20°), as for substation *D* (≈ 9°) and *C* (≈ 5°). Additionally, substations *A*, *C*, *E* and *I* have multiple line connections (see Table 3, column "n lines"). Substations *B*, *F*, *G* and *H* are located at the edge of their respective grid sections, increasing their susceptibility to elevated GICs [16].

Table 3 – Parameters of substations where max. |GIC| > 95th percentile for both events

			Event 1			Event 2		
ID	n lines	total length $[km]$	max. |GIC| [A]	$\lvert\vec{E}\rvert$ $[V/km]$	max. |GIC| lines [A]	max. |GIC| [A]	$\lvert\vec{E}\rvert$ $[V/km]$	max. |GIC| lines [A]
A	10	817.26	5.70	0.057	3.94	24.83	0.149	11.80
B	2	113.31	7.23	0.068	3.62	23.87	0.207	11.94
C	5	326.17	6.48	0.060	11.69	13.07	0.109	9.75
D	4	449.81	7.82	0.077	2.92	15.27	0.139	3.87
E	4	394.02	6.22	0.060	3.24	19.05	0.185	11.32
F	3	104.14	10.44	0.073	4.53	15.54	0.176	7.11
G	1	35.79	9.08	0.062	9.08	17.59	0.122	17.59
H	2	77.40	10.69	0.075	5.35	13.33	0.098	6.66
I	16	360.00	6.30	0.075	8.61	14.24	0.172	12.74
J	8	646.44	1.66	0.115	2.5	2.22	0.253	8.71

For Event 2, high GIC amplitudes are particularly evident in eastern Germany, especially between the states of Saxony and Brandenburg near the Polish border, where numerous lines are oriented approximately west-east. The fact that substation *B* is connected to a line extending into Poland, which was not included in the modelling, could explain the high amplitudes. To investigate this, we modelled GICs assuming a constant electric field of 1 V/km in both east and north directions with and without the first connected substations in the neighbouring countries. The result shows that including the neighbouring substations reduces the GIC amplitude at substation *B* by approximately 15% for northward $\vec{E}$, and by 50% for eastward $\vec{E}$. Other nearby substations with high amplitudes were not significantly affected. This reinforces the importance of including all neighbouring connections to avoid overestimating GICs.

Although the $\vec{E}$ magnitudes at a single point do not represent the entire $\vec{E}$ induced along the lines (which was considered in the GIC modelling), they provide a visual indicator of the observed $\vec{E}$ in that region. Examining the vectors in Figures 2-4, it is evident that the largest

GICs do not necessarily occur where large $\vec{E}$ magnitudes are present. Moreover, the substations experiencing the highest $\vec{E}$ magnitudes (Figure 1) are not among those nine with the highest GICs in either event, supporting the conclusion that $\vec{E}$ alone is not sufficient to determine if high GICs will flow at specific substations or not. One such example is substation *J* (*Eula*), marked in Figure 4, where high GIC levels might be expected but are not observed. Despite being connected to eight lines (totalling 646.44 km) and exposed to $\vec{E}$ amplitudes within the top 10% for both events – with directions closely aligned to one of the connected lines (Figure 5) – high GICs do not flow through this substation. While its lines experience GICs as high as 2.5 A for Event 1 and 8.71 A for Event 2, values comparable to those reported in Table 3 (columns "max |GIC| lines"), the combined currents entering or leaving the substation result in a lower GIC at its transformer neutral point. Since substation *J* is directly connected to *D*, the higher $\vec{E}$ magnitudes in the vicinity of *J* can be associated to the high GICs observed at *D*. This indicates that factors like long lines, numerous connections, or high GICs on individual lines do not necessarily imply elevated GIC risk at the substation. Rather, the overall configuration and orientation of the connected lines play a critical role.

Our analyses suggest that nine substations (labelled in Figure 4) are at elevated risk from space weather activity and would represent suitable locations for further analysis and monitoring. However, changes in the grid configuration will influence the GIC outcome, as evidenced by the differing GIC results for SGM 2023 and 2024 (Figure 2), and must be considered.

Finally, some grid parameters had to be assumed, introducing a potential source of modelling uncertainty. For example, raising all grounding resistances to 0.2 Ω leads to a reduction in the peak GIC by approximately 22% in both events. While higher resistances are generally expected to reduce GIC magnitudes, the actual values at each substation could either be higher or lower than assumed. It also remains unknown how grounding resistances vary between substations, or which transformers are grounded. Further analyses are needed to quantify the sensitivity of the results to variations in the grid parameters.

Acknowledgements

The results presented in this study rely on data collected at magnetic observatories. We thank the national institutes that support them and INTERMAGNET for promoting high standards of magnetic observatory practice (www.intermagnet.org). We thank the GFZ German Research Centre for Geosciences for providing the Hp30 index. Map data copyrighted OpenStreetMap contributors and available from https://www.openstreetmap.org.

Bibliography

[1] Pick L, Effenberger F, Zhelavskaya I, Korte M. A Statistical Classifier for Historical Geomagnetic Storm Drivers Derived Solely from Ground-Based Magnetic Field Measurements. Earth and Space Science. Earth and Space Science. 2019 Oct; 6(10):2000–15 https://doi.org/10.1029/2019EA000726

[2] Eastwood JP, Biffis E, Hapgood MA, et al. The Economic Impact of Space Weather: Where Do We Stand? Risk Analysis. 2017 Feb; 37(2):206–18. https://doi.org/10.1111/risa.12765

[3] Boteler DH, Pirjola RJ. Modeling geomagnetically induced currents. Space Weather. 2017 Jan; 15(1):258–76. https://doi.org/10.1002/2016SW001499

[4] Molinski T. Why utilities respect geomagnetically induced currents. Journal of Atmospheric and Solar-Terrestrial Physics. 2002 Nov; 64(16):1765–78. https://doi.org/10.1016/S1364-6826(02)00126-8

[5] Gaunt CT, Coetzee G. Transformer failures in regions incorrectly considered to have low GIC-risk. In: 2007 IEEE Lausanne Power Tech; Lausanne, Switzerland; 2007, p. 807-12. https://doi.org/10.1109/PCT.2007.4538419

[6] Carvalho AG, Pick L, Tenbohlen S, Elfert T. Modelling Geomagnetically Induced Currents in the German Transmission Grid for 2023 Geomagnetic Storms. In: VDE Hochspannungstechnik; 5. ETG-Fachtagung. 2024 Nov 11-13; Berlin, Germany; 2024; p. 62-67. Available from: https://ieeexplore.ieee.org/abstract/document/10931011

[7] Grayver A, Munch FD, Kuvshinov AV, et al. Joint inversion of satellite-detected tidal and magnetospheric signals constrains electrical conductivity and water content of the upper mantle and transition zone. Geophysical Research Letters. 2017 Jun; 44(12):6074–81. doi:10.1002/2017GL073446.

[8] Grayver A. Global 3-D Electrical Conductivity Model of the World Ocean and Marine Sediments. Geochemistry Geophysics Geosystems. 2021 Sep; 22(9). https://doi.org/10.1029/2021GC009950

[9] Tesauro M, Kaban MK, Sierd Cloetingh. EuCRUST-07: A new reference model for the European crust. Geophysical Research Letters. 2008 Mar; 35(5). https://doi.org/10.1029/2007GL032244

[10] Grayver AV, Kolev TV. Large-scale 3D geoelectromagnetic modeling using parallel adaptive high-order finite element method. GEOPHYSICS. 2015 Nov 1;80(6): E277–91. https://doi.org/10.1190/geo2015-0013.1

[11] Kruparova O, Krupar V, Szabo A, et al. Unveiling the Interplanetary Solar Radio Bursts of the 2024 Mother's Day Solar Storm. The Astrophysical Journal Letters. 2024 Jul; 970(1):L13. https://doi.org/10.3847/2041-8213/ad5da6

[12] Yamazaki Y, Matzka J, Stolle C, et al. Geomagnetic Activity Index Hpo. Geophysical Research Letters. 2022 May; 49. https://doi.org/10.1029/2022GL098860.

[13] Viljanen A. The relation between geomagnetic variations and their time derivatives and implications for estimation of induction risks. Geophysical Research Letters. 1997 March; p-24(6). 631-34. https://doi.org/10.1029/97GL00538

[14] Static Grid Model | JAO S.A. Leading service provider for TSOs [Internet]. [cited 2025 May 5]. Available from: https://www.jao.eu/static-grid-model

[15] Halbedl T. Low Frequency Neutral Point Currents on Transformer in the Austrian Power Transmission Network [Internet]. 2019 [cited 2025 May 5]. Available from: https://www.tugraz.at/fileadmin/user_upload/tugrazExternal/83b7d5e5-91ff-43e4-aa7a-6aa30ac5c9f1/Dissertationen/_PhD_Thesis_Halbedl_Final_Print.pdf

[16] Zheng K, Boteler D, Risto Pirjola, Liu L, Becker RC, Marti L, et al. Effects of System Characteristics on Geomagnetically Induced Currents. IEEE Trans. Power Delivery. 2014 Apr; 29(2):890–8. https://doi.org/10.1109/TPWRD.2013.2281191